

## Article

# Experimental and Numerical Characterization of Non-Proprietary UHPFRC Beam—Parametric Analyses of Mechanical Properties

Younes Baghaei Osgouei <sup>1</sup>, Shahriar Tavousi Tafreshi <sup>2,\*</sup> and Masoud Pourbaba <sup>3</sup>

<sup>1</sup> Department of Construction Engineering Management, Faculty of Civil and Earth Resources Engineering, Central Tehran Branch, Islamic Azad University, Tehran 1477893780, Iran; younes.baghaei@iau.ac.ir

<sup>2</sup> Department of Civil Engineering, Faculty of Civil and Earth Resources Engineering, Central Tehran Branch, Islamic Azad University, Tehran 1477893780, Iran

<sup>3</sup> Department of Civil Engineering, Maragheh Branch, Islamic Azad University, Maragheh 5519747591, Iran; pourbaba@iau-maragheh.ac.ir

\* Correspondence: sh\_tavousi@iauctb.ac.ir

**Abstract:** Fabrication of ultra-high-performance concrete (UHPC) is costly, especially when commercial materials are used. Additionally, in contrast to conventional concrete, numerical procedures to simulate the behaviour of ultra-high-performance fibre-reinforced concrete (UHPFRC) are very limited. To contribute to the foregoing issues in this field, local materials were used in the fabrication process, while accounting for environmental issues and costs. Micro steel fibres ( $L$ : 13 mm,  $d$ : 0.16 mm, and  $f_t$ : 2600 MPa;  $L$ : length,  $d$ : diameter,  $f_t$ : tensile strength) were used in 2% volumetric ratios. Compression and indirect tests were carried out on cylindrical and prismatic beams according to international standards. To further enrich the research and contribute to the limited simulation data on UHPFRC, and better comprehension of the parameters, numerical analyses were performed using the ATENA software. Finally, nonlinear regression analyses were employed to capture the deflection-flexural response of the beams. The results were promising, indicating cost-effective fabrication using local materials that met the minimum requirements of UHPFRC in terms of compressive strength. Furthermore, inverse analysis proved to be an easy and efficient method for capturing the flexural response of UHPFRC beams.

**Keywords:** fibre-reinforced concrete; finite element modelling; mechanical properties UHPC; UHPFRC



**Citation:** Osgouei, Y.B.; Tafreshi, S.T.; Pourbaba, M. Experimental and Numerical Characterization of Non-Proprietary UHPFRC Beam—Parametric Analyses of Mechanical Properties. *Buildings* **2023**, *13*, 1565. <https://doi.org/10.3390/buildings13061565>

Academic Editors: Ahmed Senouci and Walid Maherzi

Received: 30 April 2023

Revised: 7 June 2023

Accepted: 11 June 2023

Published: 20 June 2023



**Copyright:** © 2023 by the authors. Licensee MDPI, Basel, Switzerland. This article is an open access article distributed under the terms and conditions of the Creative Commons Attribution (CC BY) license (<https://creativecommons.org/licenses/by/4.0/>).

## 1. Introduction

Ultra-high-performance concrete (UHPC) with its exceptional mechanical characteristics has gained much attention in the civil engineering industry. The addition of various fibres resolves the major brittleness issue of UHPC and tailors it for specific applications based on the type and amount of fibre used in its mix design.

Fibres can be categorized into two categories: man-made and natural fibres, which are sub-divided into two and three categories as follows:

Man-made fibres: (1) inorganic: Basalt- Carbon- Glass- Steel, and (2) Polymeric: Nylon- Polyethylene (PE)- Polypropylene (PP)- Polyvinyl alcohol (PVA).

Natural fibres: (1) Plant: Coir- Sisal- etc., (2) Animal: Silk- Wool, and (3) Mineral: Asbestos- Wollastonite. Tables 1–3 show the mechanical properties of fibres, their cost, and performance when incorporated into cementitious composites.

Discontinuous steel fibres are the most widely used ones. The main purpose of adding steel fibres is to enhance both ductility and toughness. Straight steel fibres have higher contact angles, which make the fibres hydrophobic and hence result in weaker interfacial/matrix bond. For this reason, steel fibres with various geometries are used to counter this disadvantage.

Conflicting studies exist in the literature which, on one hand, emphasize the better performance of smooth micro steel (MS) fibres, while others have concluded that deformed steel fibres outperform MS fibres in almost all mechanical properties [1]. Higher aspect ratios and volumetric contents contribute to the improvement of the mechanical properties, except for the compressive strength, for which a minimal increase in compressive strength has been reported.

Man-made fibres are mainly supplied in masses, while it is common to express the performance of fibre-incorporated cementitious composites in volumetric ratios. Steel, PET (Polyethylene terephthalate), glass, basalt, and acrylic fibres are cheaper than PVA, among which steel and glass fibres offer satisfactory mechanical performance according to the available literature [2]. On a volumetric basis, nonetheless, steel, and basalt fibres offer higher densities and are therefore less favourable.

**Table 1.** Mechanical properties of various fibres [3].

Fibre Type	Diameter ( $\mu\text{m}$ )	Length (mm)	Density ( $\text{g}/\text{cm}^3$ )	Young's Modulus (GPa)	Elongation (%)	Melting/Decomposition Temperature ( $^{\circ}\text{C}$ )
PVA	39	8–12	1600	42.8	6	230
PBO *	13	6	5800	180–270	2.5–3.5	650
Carbon	6.8–20	3–18	525–4660	33–268	0.8–2.4	1150–1200
Steel	150–1000	13–25	350–2000	210	2–4	>1425
PE	24–38	12	1950–3000	39–100	3.1–8.0	150
Basalt	15–16	12	2230–4840	85.8–89.0	2.85–3.15	>1400
Glass	6–20	3–6	2000–4000	70–80	2.0–3.5	>1400
Aramid	12	6	3400	74	4.5	500
PET	38	12	1095	10.7	22	255
PP	12–41	6–12	850–928	2.7–9.0	7.3–30	160
Nylon	8	19	966	6	18	220

\* PBO: Poly (*p*-phenylene-2, 6-benzobisoxazole).

**Table 2.** Cost and performance of different fibres [3].

Fibres	Crack Width ( $\mu\text{m}$ )	Cost	Other Information
Aramid	10–30	High	Structural, low ductility
Basalt	-	Low	Structural, low ductility
Carbon	-	High	Structural, low ductility. Self-sensing
Glass	-	Low	Structural, low ductility
Nylon	>100	Comparable to PVA	Structural, high ductility
PBO	10–30	High	Structural, low ductility. high strength
PE	50–150	High	Structural, high ductility. High strength
PET	150–200	Low	Non-structural
PP	70–260	Low	Structural, high ductility. low strength
PVA	<100	-	General structural applications
Steel	10–30	High	Structural, low ductility. High strength

Note: Cost is with reference to that of PVA.

**Table 3.** Performance of steel fibres incorporated in cementitious composites [3].

Ref.	Geometrical Parameters			Volume (%)	Tensile Performance	
	Length (mm)	Diameter ( $\mu\text{m}$ )	Shape		Strength (MPa)	Strain Capacity (%)
Li et al. [4]	6–20	150	Straight	2.3	8	0.49
Wille et al. [5]	13–30	200, 300, 380	Twisted-Hooked	2.5	12.4	0.49
Naaman [6]	30	300	Twisted	2	13.6	1.25
Maalej and Li [7]	6	150	Straight	1	4	Quasi-brittle

Table 3. Cont.

Ref.	Geometrical Parameters			Volume (%)	Tensile Performance	
	Length (mm)	Diameter ( $\mu\text{m}$ )	Shape		Strength (MPa)	Strain Capacity (%)
El-Tawil [8]	30	300, 380	Twisted-Hooked	2	8.7	0.52
Tran and Kim [9]	30	300, 375	Twisted-Hooked	1	6	0.50
Kanakubo [10]	15	200	Straight	2	12.4	0.09
Naaman and Homrich [11]	30	500	Deformed-Hooked	12	28	1.00–2.00

Fibre-reinforced UHPC, also known as ultra-high-performance fibre-reinforced concrete (UHPRFC), demonstrated exceptional performance under various loadings such as compressive [12–14], tensile [15–17], shear [18–20], flexural [21–23], torsional [24,25], fatigue [26,27], and seismic loadings [28,29], as well as in terms of durability [30,31], freeze-thaw [32,33], corrosive environments [34,35], cryogenic temperatures [36,37], elevated temperatures [38,39], fracture parameters [40,41], etc. UHPRFC can also be used for strengthening purposes [42,43] and repair applications [44,45]. From another perspective, using high amounts of cementitious materials, or low water-to-cement ratios as low as 0.16, can lead to higher autogenous shrinkage [46]. Additionally, the addition of fine products such as quartz powder can lead to higher prices [47]. Researchers have added coarse aggregates with a size between 5–19 mm to UHPC to achieve the desired properties without using much cementitious materials or fine aggregates [48–51]. Given the afore-mentioned favourable properties of UHPC, extensive research has been conducted to characterize its behaviour under various loading scenarios, some of which will be briefly discussed.

Studies by Yoo et al. [52] on UHPRFC beams with various types of straight, end-hooked, and twisted steel fibres in overall volumetric ratios of 2% showed that short straight fibres ( $L$  : 19.5 mm length,  $d$ : 0.2 mm diameter) exhibited the highest flexural strength equal to 50.9 MPa, making them a more cost-effective choice compared to hybrid micro and macro fibres. In the study conducted by Meng et al. [53], normal curing conditions led to a compressive strength of 120 MPa, and the cost per 1 m<sup>3</sup> per flexural strength gain was \$4.1–\$4.5. A life cycle assessment carried out by Dong et al. [1] on a bridge revealed that the long-term performance of UHPRFC is much better and much more beneficial than conventional concrete, with a reduction in CO<sub>2</sub> emissions by 48%.

The objective of this research is to assess the flexural properties of UHPRFC beams with 2% micro steel fibre (by volume), which is the most common reinforcing material for UHPCs. The research aims to draw an analogy between the so-called flexural properties under different types of loading, namely the four-point bending test (4PBT) and three-point bending test (3PBT). Additionally, a comparative cost analysis is conducted for the production of UHPRFC. It is also noteworthy that numerical simulation of UHPRFC beams is limited in the literature, which enables us to carry out extensive sensitivity and parametric analyses, which will be discussed in the subsequent sections.

## 2. Experimental Program

### 2.1. Materials

Type II Portland cement, sieved silica fume with a maximum size of 239 nm, polycarboxylate-based (Type F) superplasticizer [54], silica sand no finer than sieve No. 200 (0.074 mm), and micro steel fibres ( $L$ : 13 mm,  $d$ : 0.16 mm, and  $f_t$  : 2600 MPa;  $L$  : length,  $d$ : diameter,  $f_t$  : tensile strength) were used in 2% volumetric ratios. Figure 1 shows the superplasticizer, silica fume, silica sand, and steel fibres used in this study. According to ASTM C494/C494M [54], Type F superplasticizer can reduce the need for water by at least 12% and has a yellow colour. The material constituents are given in Table 4, the mix composition of materials is given in Table 5, and the specifications of the steel fibre are given in Table 6.

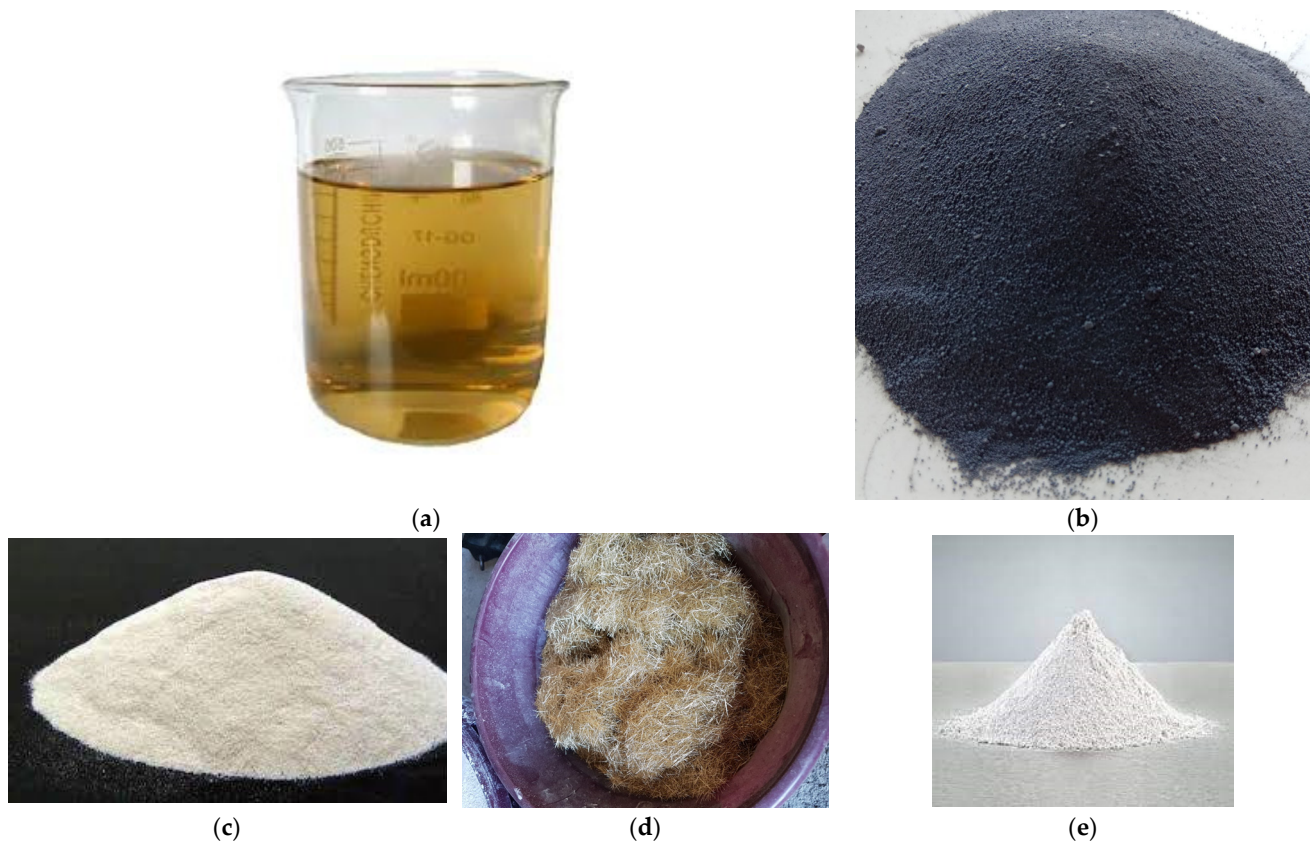


**Figure 1.** (a) Superplasticizer, (b) Silica fume, (c), Silica sand, (d) Steel fibres, and (e) Silica flour.

**Table 4.** Material composition of cement and silica fume.

	Cement	Silica Fume
CaO	61.33	0.38
Al <sub>2</sub> O <sub>3</sub>	6.40	0.25
SiO <sub>2</sub>	21.01	96
Fe <sub>2</sub> O <sub>3</sub>	3.12	0.12
MgO	3.02	0.10
SO <sub>3</sub>	2.30	-
Specific surface area (cm <sup>2</sup> /g)	3413	200,000
Density (g/cm <sup>3</sup> )	3.15	2.10

**Table 5.** Mix composition.

W/B	Unit Weight (kg/m <sup>3</sup> )					
	Water	Cement	Silica Fume	Silica Sand	Silica Flour	Superplasticizer
0.2	160.3	788.5	197.1	867.4	236.6	52.6 *

\* Superplasticizer includes 30% solid (15.8 kg/m<sup>3</sup>) and 70% water (36.8 kg/m<sup>3</sup>).

**Table 6.** Properties of steel fibre.

Type	L (mm)	D/W (mm)	f <sub>t</sub> (MPa)	E (GPa)
Straight micro steel (MS)	13	0.16	2700	200

Note: L: Length; D/W: Diameter/Width; f<sub>t</sub> (MPa): Tensile strength; E: Modulus of Elasticity.

## 2.2. Mixing Procedure

Silica fume and silica sand were initially mixed for 5 min before the addition of cement and silica flour. Thereafter, mixing continued for another 5 min before the addition of water in a gradual manner. To improve flowability, superplasticizer was added gradually as well. Steel fibres were added manually as the mixer mixed the composition. The process of the experiment is presented in Figure 2. Specimens were removed from the formwork after 1 day and were cured under normal conditions in water.

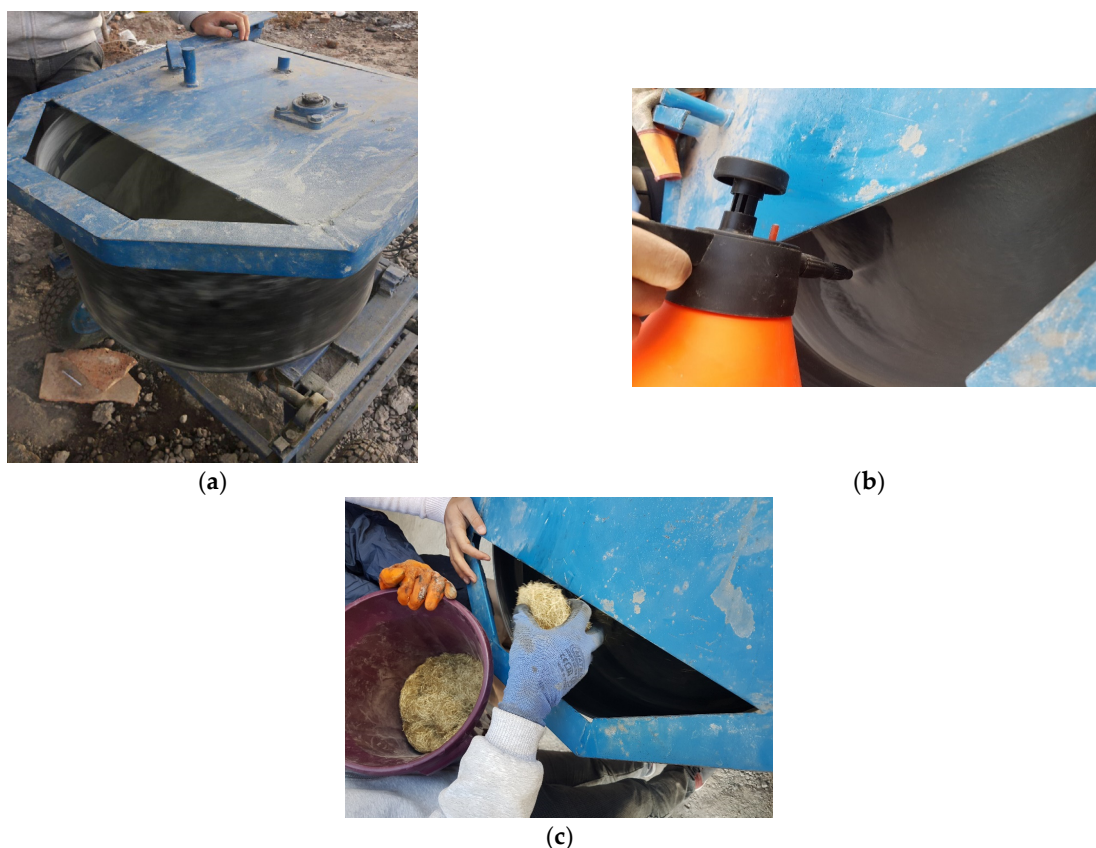


**Figure 2.** (a) Mixer, (b) Gradual addition of water, and (c) Gradual addition of steel fibres.

### 2.2.1. Compression Tests

Displacement-controlled loading with a rate of 1 mm/min was applied to  $100 \times 100 \times 200$  mm cylindrical UHPFRs according to ASTM C39/C39M [55]. A minimum of 175 MPa value was achieved based on the average of three test specimens, which satisfies the regulations of UHPC [56]. The cracking pattern of the cylindrical specimen is shown in Figure 3. Due to the presence of MS fibres, the integrity of the specimen has been completely maintained, with cracks parallel to the specimen only in regions close to the loading surface.



**Figure 3.** Cracking pattern of the cylindrical specimen with 2% MS fibre.

### 2.2.2. Flexural Tests

Regulations of ASTM C1609/C1609M [57] were adopted to apply flexural loading to eight UHPFRC beams with dimensions of  $100 \times 100 \times 500$  mm (clear span: 450 mm), as shown in Figure 4. Linear variable displacement transducers (LVDT) were used to monitor deflection values. The average value of the load-deflection response was presented in this study.

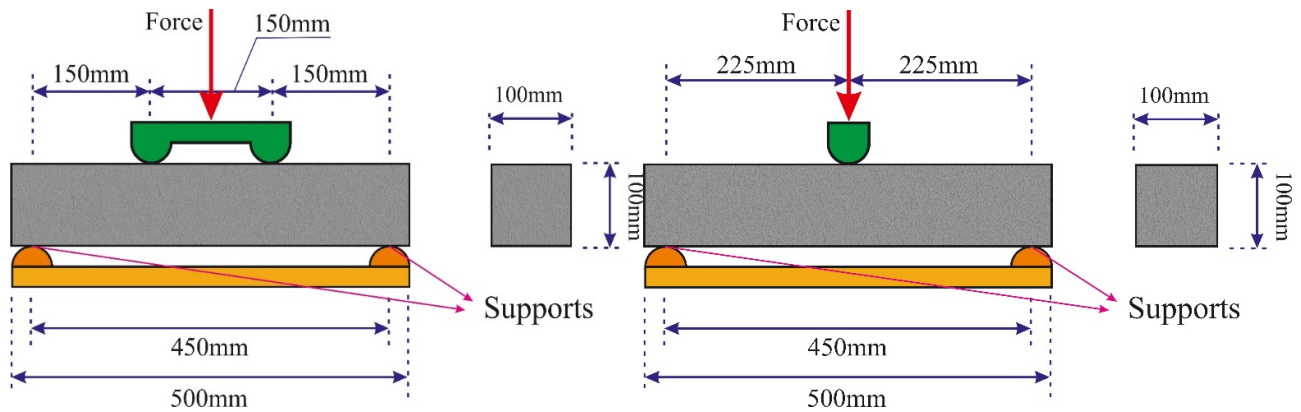


Figure 4. Four-point and three-point loading setups.

### 3. Numerical Analysis

The ATENA software [58], a finite element software specifically developed for concrete structures, was used within the GID software [59] environment as a module to simulate the UHPFRC beams. This software has been extensively used to simulate normal-strength concrete [60,61] and fibre-reinforced concrete [62–64].

With the knowledge that testing UHPFRC specimens under direct tension is challenging, inverse analysis is a good alternative to derive the direct tensile curve from flexural loading test. This method has been previously used by the authors [65–69]. The main concept relies on finding the mid-span deflection values, where differences between the numerical curve and the experimental curve are noticeable and updating the initially defined tensile stress-tensile strain curve based on the user's experience at the strain values corresponding to the above-mentioned deflections. Correlation between fracture strain and deflections is possible by monitoring crack mid-span crack widths using Equation (1):

$$\varepsilon = \frac{w}{L_t} \quad (1)$$

where  $\varepsilon$  is the fracture strain;  $w$  is the crack width and  $L_t$  is the characteristic length. For further information, the reader is referred to the ATENA documentation [58]. The Cementitious2User material model was used to simulate concrete, while a bi-linear strain hardening material model was used for steel supports and steel plates with a thickness of 20 mm. Newton-Raphson method was used to solve the nonlinear set of equations.

It is noteworthy that the tensile strength and modulus of elasticity of UHPFRC were estimated based on the equation given by Wille et al. [5] and Suksawang et al. [70] as expressed in Equations (2) and (3), where  $f_t$  is the tensile strength,  $V_f$  is the volumetric ratio of steel fibres, and  $E$  is the modulus of elasticity of UHPFRC:

$$f_t = -\left(V_f - 4\right)^2 + 14 \quad (2)$$

$$E = 4700\lambda\sqrt{f'_c} \quad \lambda = \left(1 + 0.7V_f\right)/2 \quad (3)$$

Tensile function and the comparison of experimental and numerical results are given in Figure 5, which indicates favourable agreement between them.

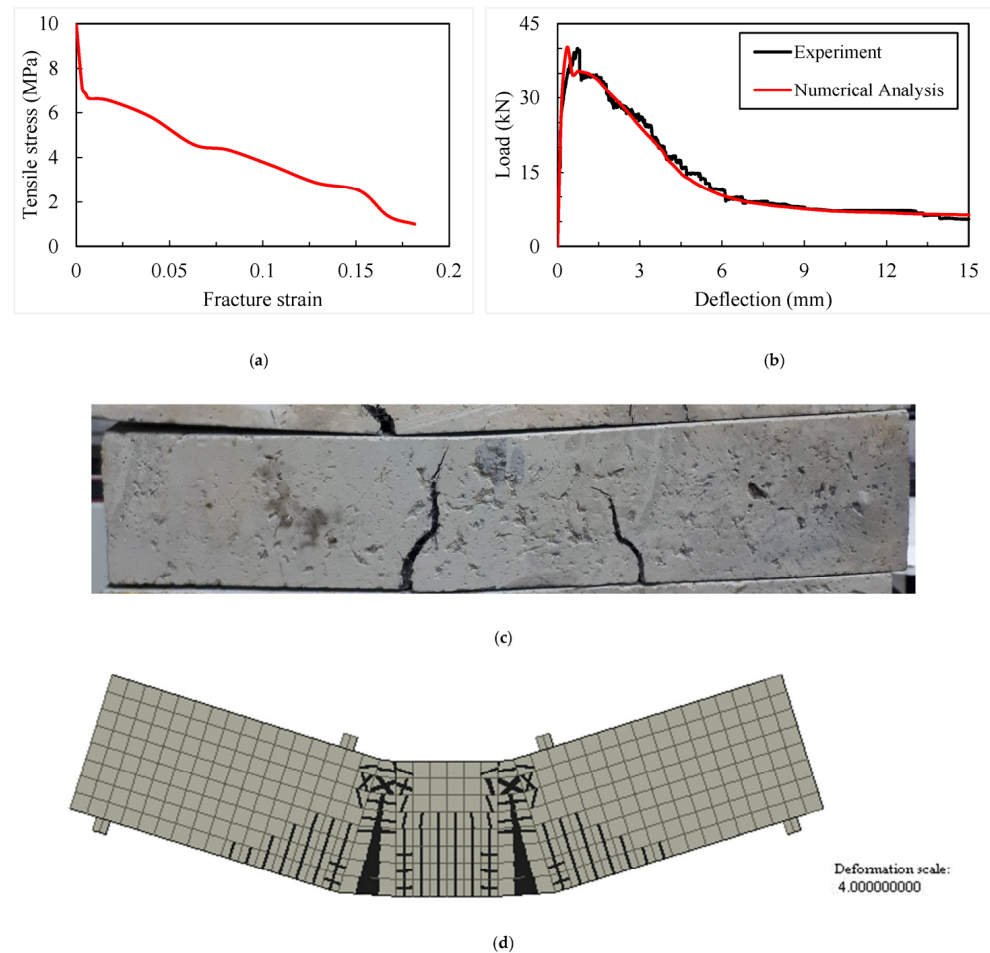


**Figure 5.** Experimental and numerical results (a) Tensile function for UHPFRC, (b) comparison of experimental and numerical flexural-load deflection curves, (c) experimental crack pattern, and (d) numerical crack pattern.

## 4. Results and Discussions

### 4.1. Sensitivity Analyses

Various sensitivity analyses were carried out on different parameters to recognize the key ones, including compressive strength, mesh size, tensile strength, and modulus of elasticity. The following sections discuss these analyses in detail.

#### 4.1.1. Mesh Size

Four different mesh sizes, namely 16.7 mm, 12.5 mm, 10 mm, and 8.3 mm, were chosen to investigate the effect of mesh size on the flexural response of the beam and verify mesh convergence. The result is shown in Figure 6a,b. It is observed that a finer mesh leads to a stiffer flexural response. By increasing the mesh size from 16.7 mm–8.3 mm, the response became 1.49%, 6.25%, and 8.52% stiffer. This issue can be justified by the fact that according to the documentation of ATENA [58], finer mesh means smaller characteristic length values, which in turn result in smaller crack widths according to Equation (1). Therefore, the response becomes stiffer.

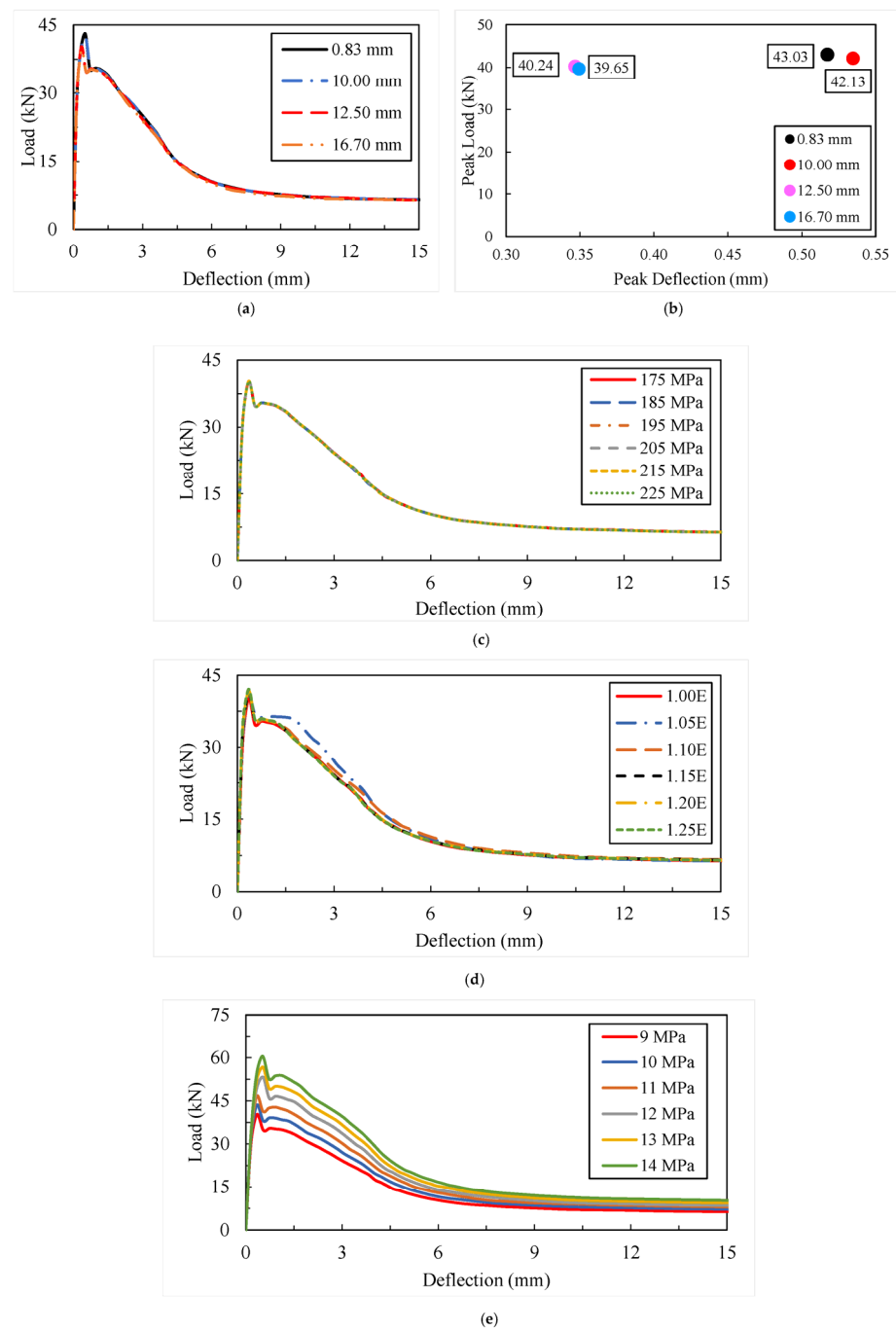


**Figure 6.** (a) Peak load vs. deflection, and sensitivity analyses with regard to (b) mesh size, (c) compressive strength, (d) modulus of elasticity, and (e) tensile strength of UHPFRC beams under 4PBT.

#### 4.1.2. Compressive Strength

The results given in Figure 6c show that variation in compressive strength has almost no effect on the response of the beam. This can be largely explained by the high compressive strength of UHPCs. As shown in Figure 7, the compressive stresses are well below the compressive capacity of the beam. Therefore, variations in this parameter practically make no changes to the overall response.

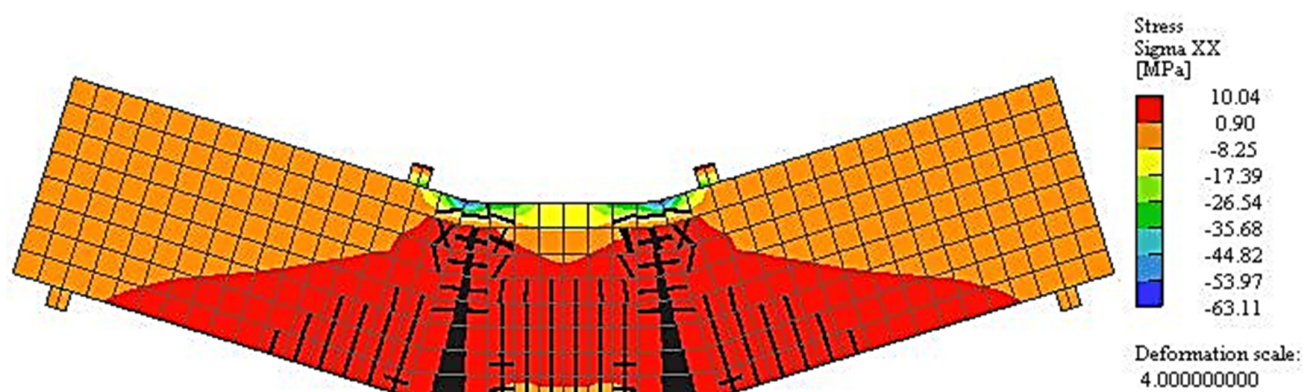


Figure 7. Stress contour for the  $100 \times 100 \times 500$  mm beam with  $f_t = 14$  MPa.

#### 4.1.3. Modulus of Elasticity

Changes in the modulus of elasticity, as given in Figure 6d, lead to a stiffer response of the beam in both the linear and nonlinear branch of the flexural load-deflection curve. Increasing the modulus of elasticity from  $1.0 E$  to  $1.25 E$  led to an increase of 1.02%, 2.01%, 2.96%, 3.75%, and 4.62%, respectively. However, it is observed that the effect of the modulus of elasticity is insignificant.

#### 4.1.4. Tensile Strength and Crack Width

It is obvious from Figure 6e that the tensile strength has the most notable effect on the overall response of the beam, and as expected, it contributes to higher peak load values with its increase. Improvements to 8.19%, 15.75%, 32.25%, 40.90%, and 50.25% were observed when the tensile strength varied between 9–14 MPa. It is worth mentioning that Figure 7 further corroborates the result for the sensitivity of the compressive strength, as even higher compressive stresses are well below the compressive strength of the concrete.

#### 4.2. Size Effect, Fracture Energy, and Failure Pattern in 4PBTs

Two cases were considered for the size effect: variations in height (150 mm, 200 mm) (2) and variations in the overall size of the beam ( $200 \times 200 \times 1000$  mm,  $300 \times 300 \times 1500$  mm, and  $400 \times 400 \times 2000$  mm). As expected, variation in geometrical parameters significantly affect the flexural load-deflection response of the beams. For a given length and width, variation in the depth of the beam contributes to a 130% and 295% increase in the peak load, occurring at higher deflections (Figure 8a). Similarly, an overall increase in size by 2, 3, and 4 times increased the peak load by 280%, 730%, and 1267%, respectively (Figure 8b). Deflection softening occurred more rapidly in beams with larger effective depths. The underlying reason is the larger amount of energy released upon cracking of concrete. For overall variations in geometrical dimensions, the variations were less pronounced.

A similar but less pronounced trend was also observed for the increasing trend of fracture energy at  $L/30$  clear-span ratio of the beams (Figure 9). It should be highlighted that comparing Figures 9c and 10 shows that more than 90% of the energy absorption takes place in the post-peak branch, which denotes the ductility of UHPFRC beams. Accordingly, according to Figure 11, an increase in the tensile strength of UHPFRC results in the improvement of fracture energy, with the rate decreasing as the tensile strength increases. Figure 12 presents the scanning electron microscopy (SEM) images of fibres in the concrete mix; it can be seen that failure is mainly characterized by the fracture of fibres, as their cross-section is oblique or deformed.

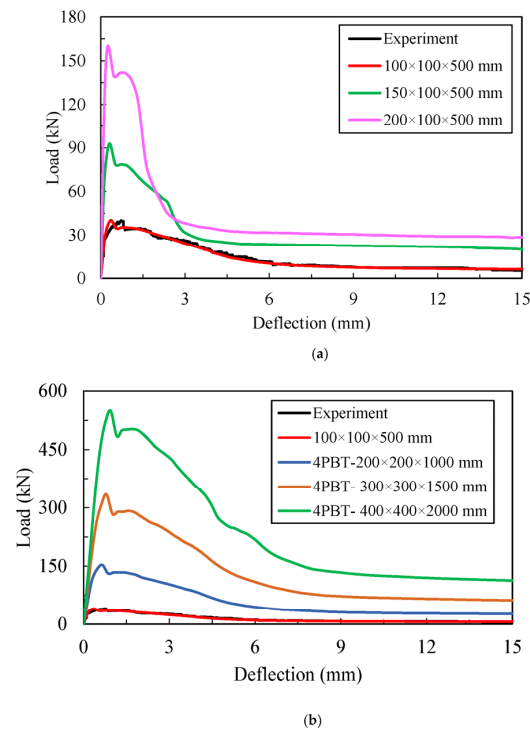


Figure 8. Flexural load-deflection response (a) depth effect, and (b) overall size effect.

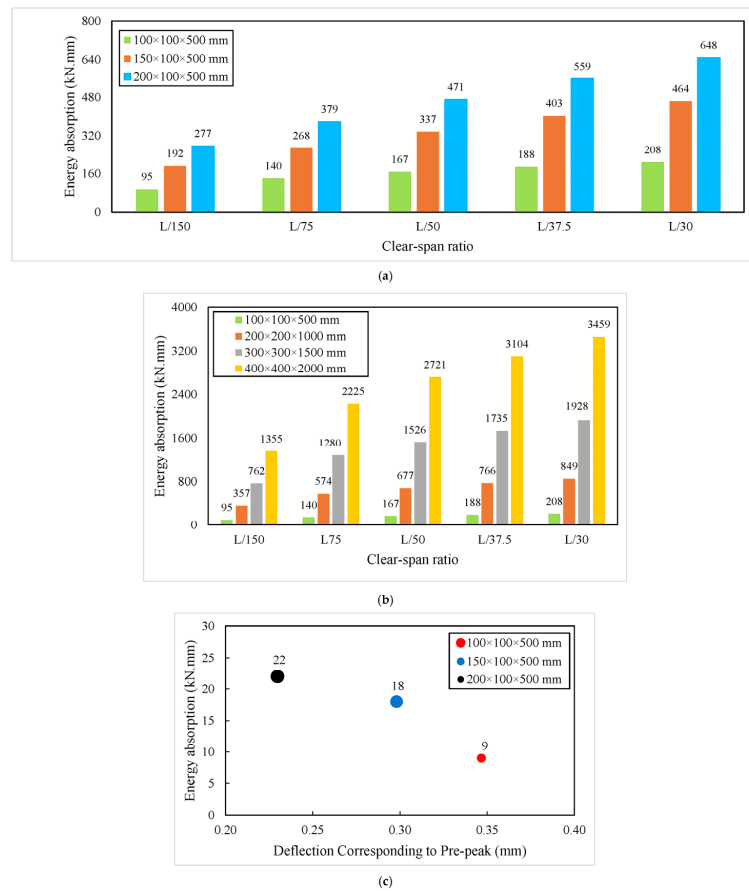


Figure 9. Energy absorption with regard to (a) depth variations, (b) overall size variations, and (c) depth variation in the pre-peak branch of UHPFRC beams under 4PBT.

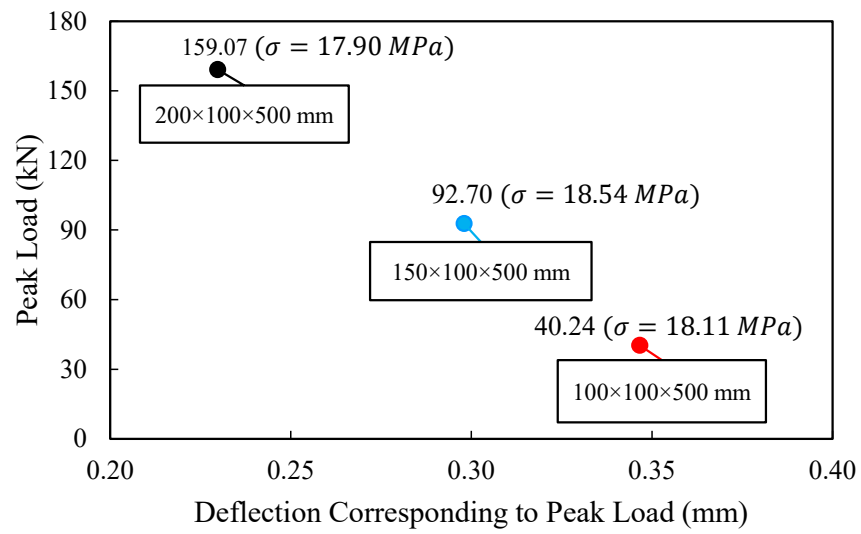


Figure 10. Effect of depth variation on peak flexural load-deflection values of UHPFRC beams under 4PBT.

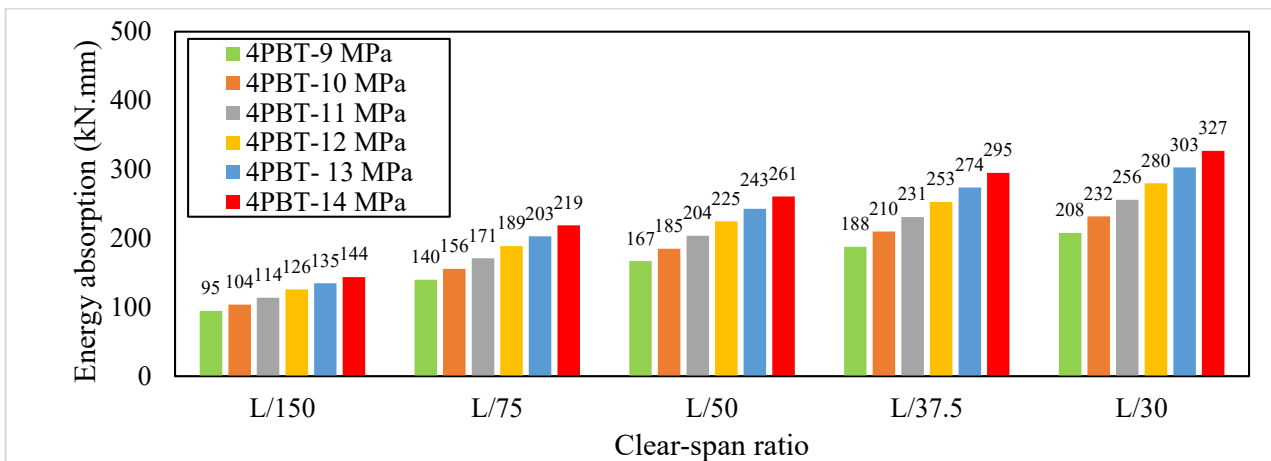


Figure 11. Sensitivity of energy absorption with respect to tensile strength at various clear-span ratio under 4PBT.

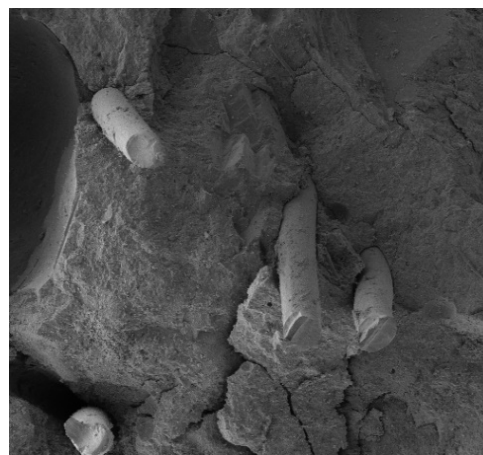
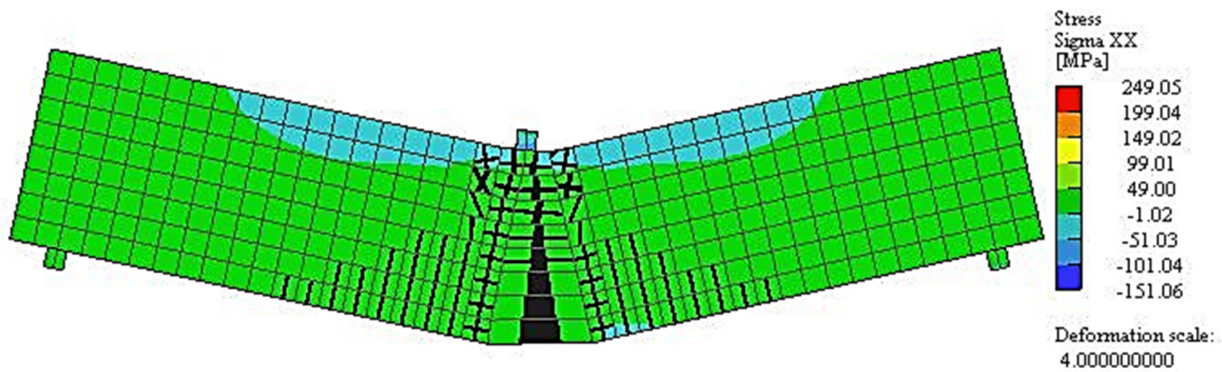


Figure 12. SEM image of steel fibres in the concrete mix.

### 4.3. Three-Point Bending

Three-point bending tests were also simulated based on the setup given in Figure 4. They have been presented for comparative purposes with their 4PBT counterpart. Unlike 4PBT, where the maximum moment occurs within a large region, allowing for easier computer simulation and uniform stress, in 3PBTs, the localization of cracks occurs under the applied load (Figure 13). As a result, the absorbed energy is greater in 4PBT. Analogies between flexural load-deflection response under 3PBT and 4PBT, as well as the sensitivity analysis of tensile strength, are given in Figure 14, which is comparable to its 4PBT counterpart, as well as its stress contour (Figure 15). Energy absorption values for 3PBT are given in Figure 16a. Similarly, energy absorption values at different clear-span ratios, size effect, and under 3PBT are given in Figure 16b. It can be seen that energy absorption values are lower than those of 4PBTs, and owing to the localization of crack under 3PBT.



**Figure 13.** Stress contour for the  $100 \times 100 \times 500$  mm beam with  $f_t = 9$  MPa under 3PBT.

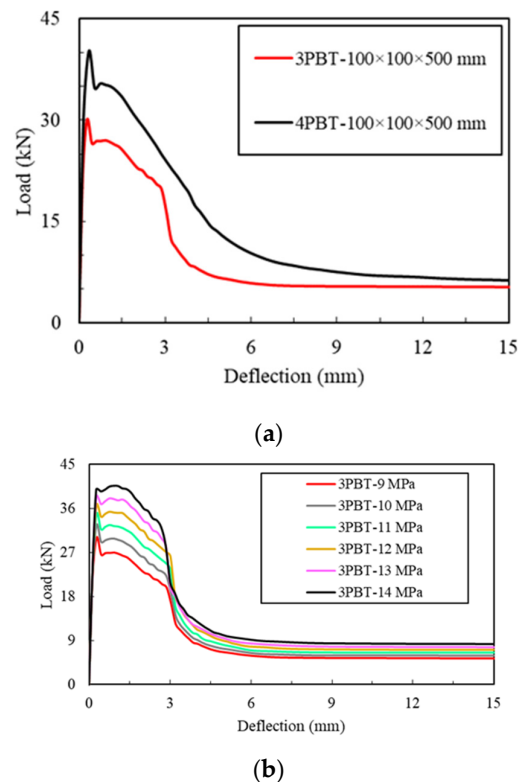


**Figure 14.** Load-deflection response (a) comparison of 3PBT and 4PBT, and (b) sensitivity to tensile strength in 3PBT.

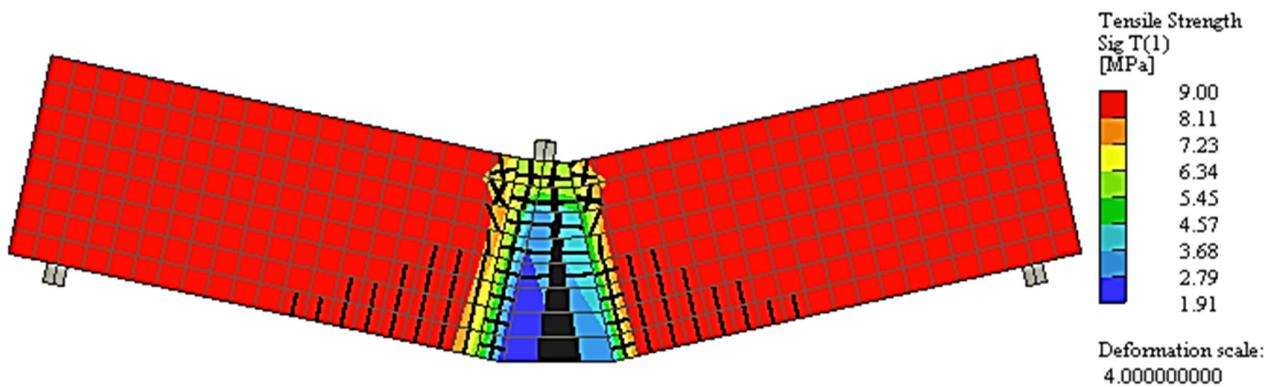
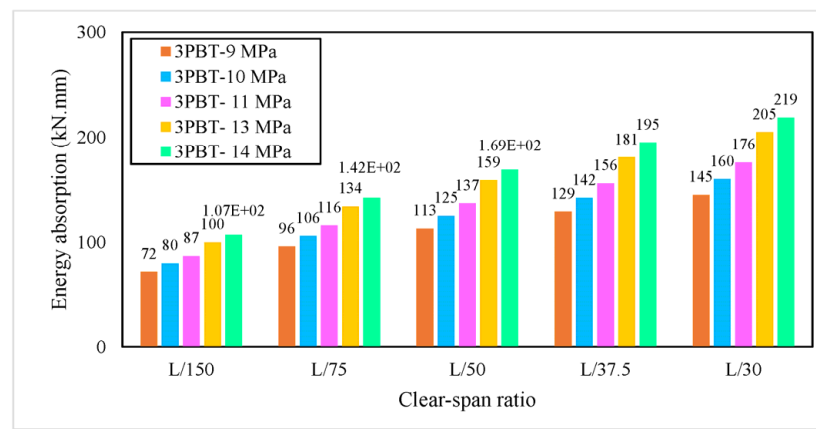
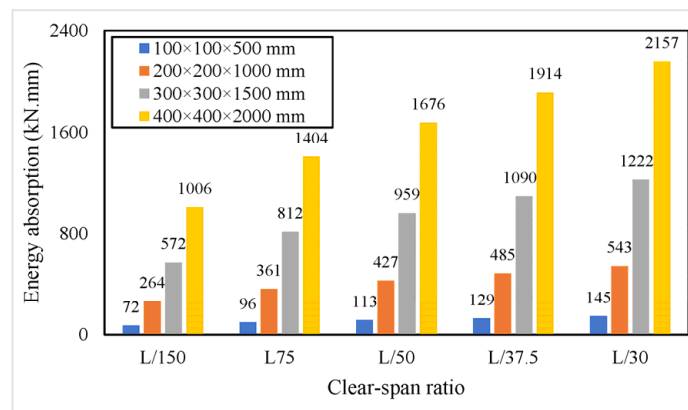


Figure 15. Tensile stress contour for the 100 × 100 × 500 mm beam with  $f_t = 9$  MPa under 3PBT.



(a)



(b)

Figure 16. Energy absorption sensitivity to (a) tensile strength, and (b) overall size in various clear-span ratios.

#### 4.4. Modelling of Size Effect

Three well-known size effect models given in Equations (4)–(6) [71–73] were used to account for the size effect in test specimens, where  $\beta$ ,  $d_0$ ,  $A$ ,  $B$ ,  $\alpha$  are regression parameters, and  $f$  is the tensile strength.

$$\sigma_N = \frac{\beta f}{\sqrt{1 + \beta}} \quad \beta = \frac{d}{d_0} \tag{4}$$

$$\sigma_N = F\sqrt{A + B/d} \tag{5}$$

$$\sigma_N = \frac{\beta f}{\sqrt{1 + \beta}} + \alpha f \quad (6)$$

Figure 17 clearly shows the size effect in beams (i.e., the stress reduces with an increase in size) with higher scatter of data in 4PBT since maximum stress is scattered within a larger area rather than a small region. Furthermore, parameter  $d_0$  in Equation (4) is a measure of brittleness. Based on Table 7, it is observed that values of  $d_0$  for 3PBT are lower than its 4PBT, which means under 3PBT, the specimen shows a more brittle manner, as energy absorption values give credence to it.

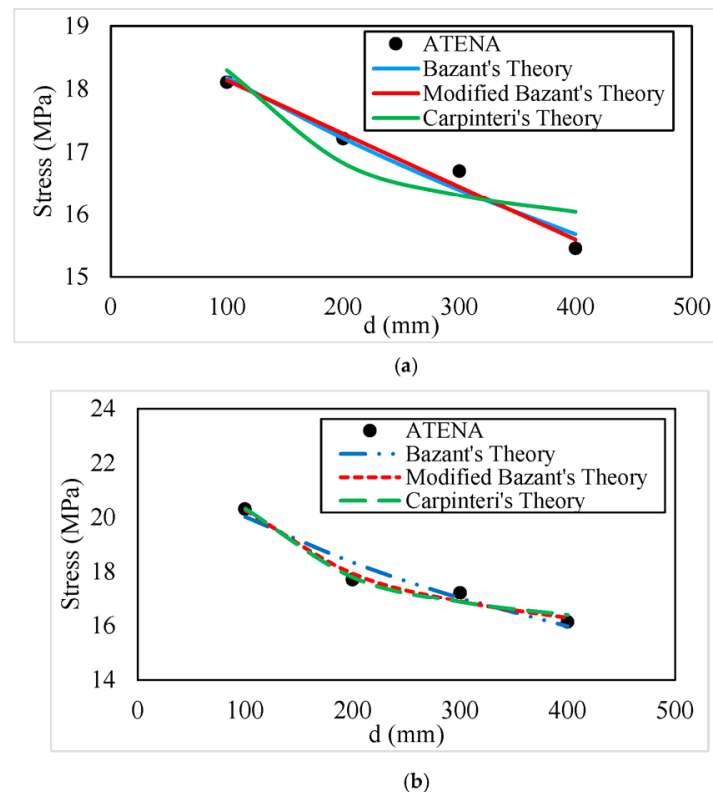


Figure 17. Size effect for UHPFRC beams (a) 4PBT, and (b) 3PBT.

Table 7. Fitting parameters size effect theories.

Sample ID	Bazant and Chen [71]			Kim and Yi [73]				Carpinteri and Chiaia [72]		
	B	$d_0$	$R^2$	B	$d_0$	$\alpha$	$R^2$	A	B	$R^2$
4PBT	2.146	772.514	0.960	2618.805	1,390,098	−2616.700	0.9753	231.460	10,326.170	0.815
3PBT	2.473	424.179	0.941	14.241	0.390	1.3648	0.981	220.435	19,266.440	0.979

#### 4.5. Cost Analysis

The cost efficiency of UHPFRC was evaluated by analysing the respective price of its constituents, considering that long-term performance should be the criterion rather than the short-performance. According to Dong [1], UHPFRC is resilient and cost-effective in the long term. The overall cost of UHPFRC is given in Table 8. For an analogy, short fibres cost 3.554 €/kg in Korea, while ultra-short fibres utilized by Skazlic' and Bjegović [74] and fibres used by Walraven [75] amounted to 3.223 €/kg. Based on Table 8, the overall cost of UHPFRC is lower in Iran.

**Table 8.** Cost of each component of UHPFRC.

Material	Price per kg (Rial)
Portland Cement	3500
Silica Sand	1000
Silica Fume	12,000
Quartz Powder	15,000
Superplasticizer	200,000
Steel Fibre	250,000
Water	Almost free

300,000 Rials = 1 €.

## 5. Conclusions

This research presents experimental and numerical studies on eight UHPFRC beams fabricated using non-proprietary materials. The beams were tested under 4PBT, and their results were compared with those obtained through numerical analysis under 3PBT. An inverse analysis approach was employed to obtain the tensile function of the UHPFRC beams. After validation, numerous parametric analyses were carried out to determine the key parameters that govern the behaviour of UHPFRC beams. Based on the results, the salient outcomes of the present study are as follows:

- UHPFRC shows satisfactory tensile strength (i.e., 10 MPa) and ductility, provided by the inclusion of MS fibres. Failure of specimens was characterized by the rupture of MS fibres.
- The inverse analysis approach was adopted, which successfully captured the flexural response of the beams.
- Finer mesh sizes result in stiffer responses of the beams; however, the impact is insignificant.
- The model was insensitive to variations in compressive strength, as the compressive strength of the specimen is well greater than the compressive stress sustained by them. Increasing the modulus of elasticity by 25% contributed only 4.62% to the load capacity. On the other hand, tensile strength is the most important parameter, as its variation led to notable changes of up to 50.25% when changed from 10 MPa to 14 MPa in the flexural load-deflection response of the beams.
- Size variations led to significant changes in the response of the beams, with the energy absorption being the most sensitive to the changes. Doubling the effective depth led to an improvement of 295% in the load capacity, while doubling the overall dimensions led to an increase of 280%.
- Linear relationships (with  $R^2$  over 0.96) exist between the energy absorption parameter and variations of tensile strength, depth, and overall size of the beam.

Size effect was observed with depth variations as the stress value showed a declining trend. Additionally, it was observed that specimens show a more brittle manner under 3PBT compared to 4PBT.

### *Recommendation for Future Works*

The authors recommend conducting further research on UHPFRC beams with various types of fibres and dosages, larger overall dimensions matching structural dimensions, and different span-to-depth ratios to deepen the knowledge regarding the performance of UHPFRC in terms of various parameters and the feasibility of its application in real-world applications.

**Author Contributions:** Conceptualization, S.T.T. and M.P.; methodology, S.T.T.; software, Y.B.O.; validation, M.P. and Y.B.O.; formal analysis, Y.B.O.; investigation, S.T.T. and Y.B.O.; resources, Y.B.O.; data curation, S.T.T. and Y.B.O.; writing—original draft preparation, Y.B.O.; writing—review and editing, M.P.; visualization, Y.B.O.; supervision, S.T.T.; project administration, M.P.; funding acquisition, S.T.T. All authors have read and agreed to the published version of the manuscript.

**Funding:** This research received no external funding.

**Data Availability Statement:** The data related to the results of this study are available upon request from the corresponding author.

**Conflicts of Interest:** The authors declare no conflict of interest.

## References

1. Dong, Y. Performance assessment and design of ultra-high performance concrete (UHPC) structures incorporating life-cycle cost and environmental impacts. *Constr. Build. Mater.* **2018**, *167*, 414–425. [[CrossRef](#)]
2. Lu, Z.; Feng, Z.G.; Yao, D.; Li, X.; Ji, H. Freeze-thaw resistance of Ultra-High performance concrete: Dependence on concrete composition. *Constr. Build. Mater.* **2021**, *293*, 123523. [[CrossRef](#)]
3. Zhang, D.; Yu, J.; Wu, H.; Jaworska, B.; Ellis, B.R.; Li, V.C. Discontinuous micro-fibers as intrinsic reinforcement for ductile Engineered Cementitious Composites (ECC). *Compos. Part B Eng.* **2020**, *184*, 107741. [[CrossRef](#)]
4. Li, V.C.; Wu, H.C.; Maalej, M.; Mishra, D.K.; Hashida, T. Tensile behavior of cement-based composites with random discontinuous steel fibers. *J. Am. Ceram. Soc.* **1996**, *79*, 74–78. [[CrossRef](#)]
5. Wille, K.; El-Tawil, S.; Naaman, A.E. Properties of strain hardening ultra high performance fiber reinforced concrete (UHP-FRC) under direct tensile loading. *Cem. Concr. Compos.* **2014**, *48*, 53–66. [[CrossRef](#)]
6. Naaman, A.E. Engineered steel fibers with optimal properties for reinforcement of cement composites. *J. Adv. Concr. Technol.* **2003**, *1*, 241–252. [[CrossRef](#)]
7. Maalej, M.; Li, V.C. Flexural/tensile-strength ratio in engineered cementitious composites. *J. Mater. Civ. Eng.* **1994**, *6*, 513–528. [[CrossRef](#)]
8. Kim, D.J.; El-Tawil, S.; Naaman, A.E. Rate-dependent tensile behavior of high performance fiber reinforced cementitious composites. *Mater. Struct.* **2009**, *42*, 399–414. [[CrossRef](#)]
9. Tran, T.K.; Kim, D.J. Investigating direct tensile behavior of high performance fiber reinforced cementitious composites at high strain rates. *Cem. Concr. Res.* **2013**, *50*, 62–73. [[CrossRef](#)]
10. Kanakubo, T. Tensile characteristics evaluation method for ductile fiber-reinforced cementitious composites. *J. Adv. Concr. Technol.* **2006**, *4*, 3–17. [[CrossRef](#)]
11. Naaman, A.E.; Homrich, J.R. Tensile stress-strain properties of SIFCON. *Mater. J.* **1989**, *86*, 244–251.
12. Kim, J.C.; Lim, W.Y. Prediction of compressive strength and elastic modulus for ultra-high-performance concrete. *Constr. Build. Mater.* **2023**, *363*, 129883. [[CrossRef](#)]
13. Wang, B.; Liu, G.; Zhou, J. Properties of Concrete Columns Strengthened by CFRP-UHPC under Axial Compression. *Buildings* **2023**, *13*, 596. [[CrossRef](#)]
14. Zhang, X.; Lu, Y.; Wu, X.; Wang, P.; Li, R.; Liu, Y.; Shen, C.; Zhang, H.; Zhang, D. Constitutive model for ultra-high performance concrete (UHPC) considering the size effect under cyclic compressive loading. *Constr. Build. Mater.* **2023**, *368*, 130499. [[CrossRef](#)]
15. Li, J.; Deng, Z. Tensile behavior of ultra-high performance concrete reinforced with different hybrid fibers. *Struct. Concr.* **2023**, *24*, 1415–1435. [[CrossRef](#)]
16. Shi, Z.; Su, Q.; Kavoura, F.; Veljkovic, M. Uniaxial tensile response and tensile constitutive model of ultra-high performance concrete containing coarse aggregate (CA-UHPC). *Cem. Concr. Compos.* **2023**, *136*, 104878. [[CrossRef](#)]
17. Xin, T.I.; Zhi, F.A.; Teng, Z.H.; Xiang, Y. Behavior and constitutive model of ultra-high-performance concrete under monotonic and cyclic tensile loading. *Constr. Build. Mater.* **2023**, *389*, 131634.
18. Pan, R.; Song, X.; He, W.; Qin, L. Direct shear strength of UHPC considering size effect: Theoretical model and experimental verification. *J. Build. Eng.* **2023**, *2023*, 106381. [[CrossRef](#)]
19. Jiang, H.; Huang, C.; Mei, G.; Gao, X.; Tian, Y.; Sun, X. Experimental and numerical investigations on direct shear performance of UHPC dry joints. *Eng. Struct.* **2023**, *283*, 115872. [[CrossRef](#)]
20. Ye, M.; Li, L.; Yoo, D.Y.; Li, H.; Shao, X.; Zhou, C. Mechanistic understanding of precast UHPC segmental beams with external tendons and epoxy joints subject to combined bending and shear. *Eng. Struct.* **2023**, *280*, 115698. [[CrossRef](#)]
21. Cai, H.; Liu, Z.; Xu, Z.; Zhang, Z.; Xu, T. Flexural Tensile Behavior of Interface between Precast and Cast-in-Place UHPC Members Based on Four-Point Bending Test. *Buildings* **2023**, *13*, 745. [[CrossRef](#)]
22. Li, C.; Aoude, H. Effect of UHPC jacketing on the shear and flexural behaviour of high-strength concrete beams. *Structures* **2023**, *51*, 1972–1996. [[CrossRef](#)]
23. Zhang, Y.; Wang, H.; Qin, Y.; Huang, S.; Fan, W. Experimental and analytical studies on the flexural behavior of steel plate-UHPC composite strengthened RC beams. *Eng. Struct.* **2023**, *283*, 115834. [[CrossRef](#)]
24. Cao, X.; Zhang, W.J.; Ren, Y.C.; Fu, F.; Li, Y.H.; He, D.B.; Zheng, Y. Torsional capacity of ultra-high-performance concrete beams using rectangle stirrup. *J. Build. Eng.* **2023**, *69*, 106231. [[CrossRef](#)]
25. Yousef, A.M.; Marami, N.A.; Tahwia, A.M. Experimental and Numerical Investigation for Torsional Behavior of UHPFRC Shallow and Deep Beams. *Arab. J. Sci. Eng.* **2023**, *2023*, 1–4. [[CrossRef](#)]
26. Wang, J.; Ji, W.; An, M.; Li, W. Fatigue behaviour of reinforced UHPC-NC composite beams. *Case Stud. Constr. Mater.* **2023**, *2023*, e02055.

27. Li, L.; Xu, L.; Zeng, Y.; Cui, K.; Chi, Y.; Huang, L. Understanding the role of coarse aggregate on tensile fatigue behaviors of ultra-high performance concrete. *Cem. Concr. Compos.* **2023**, *2023*, 105069. [[CrossRef](#)]
28. Yan, Y.; Yan, Y.; Wang, Y.; Cai, H.; Zhu, Y. Seismic Behavior of UHPC-Filled Rectangular Steel Tube Columns Incorporating Local Buckling. *Buildings* **2023**, *13*, 1028. [[CrossRef](#)]
29. Luo, Y.; Zhao, Y.; Chen, Y.; Lin, X.; Yan, J. Experimental Studies on Seismic Performance of UHPSFRC-Filled Square Steel Tubular Columns. *Buildings* **2022**, *12*, 798. [[CrossRef](#)]
30. Hasan, M.; Jamil, M.; Saidi, T. Mechanical properties and durability of ultra-high-performance concrete with calcined diatomaceous earth as cement replacement. *J. Mech. Behav. Mater.* **2023**, *32*, 20220272. [[CrossRef](#)]
31. Amin, M.; Agwa, I.S.; Mashaan, N.; Mahmood, S.; Abd-Elrahman, M.H. Investigation of the Physical Mechanical Properties and Durability of Sustainable Ultra-High Performance Concrete with Recycled Waste Glass. *Sustainability* **2023**, *15*, 3085. [[CrossRef](#)]
32. Xie, X.; Fan, J.; Guo, P.; Huang, H.; Hu, J.; Wei, J. Composition Design and Fundamental Properties of Ultra-High-Performance Concrete Based on a Modified Fuller Distribution Model. *Materials* **2023**, *16*, 700. [[CrossRef](#)] [[PubMed](#)]
33. Xi, B.; Al-Obaidi, S.; Ferrara, L. Effect of different environments on the self-healing performance of Ultra High-Performance Concrete—A systematic literature review. *Constr. Build. Mater.* **2023**, *374*, 130946. [[CrossRef](#)]
34. Al-Huri, M.A.; Al-Osta, M.A.; Ahmad, S.; Al-Dulaijan, S.U. Effect of early-strengthening of RC beams using UHPC layers on their performance against reinforcement corrosion. *Struct. Concr.* **2023**, *24*, 2260–2279. [[CrossRef](#)]
35. El-Khoriby, R.S.; Taher, S.E.; Ghazy, M.F.; Abd-Elaty, M.A. Performance of pre-cracked beams exposed to corrosion environment cast with ultra-high performance concrete. *Ain Shams Eng. J.* **2023**, *2023*, 102171. [[CrossRef](#)]
36. He, B.; Zhang, H.; Zhu, X.; Zheng, Q.; Onuaguluchi, O.; Banthia, N.; Jiang, Z. Thermal-dependent brittleness effect of ultra-high performance concrete exposed to cryogenic flexural loads by acoustic emission evaluation. *Cem. Concr. Compos.* **2023**, *2023*, 105056. [[CrossRef](#)]
37. Zhang, H.; He, B.; Zhu, X.; Wang, Q.; Jiang, Z. Flexural performance and patterns identification of UHPC subjected to alternating elevated and cryogenic attacks with acoustic emission characterization. *Constr. Build. Mater.* **2023**, *364*, 129962. [[CrossRef](#)]
38. Amran, M.; Murali, G.; Makul, N.; Kurpińska, M.; Nehdi, M.L. Fire-induced spalling of ultra-high performance concrete: A systematic critical review. *Constr. Build. Mater.* **2023**, *373*, 130869. [[CrossRef](#)]
39. Banerji, S.; Kodur, V. Numerical model for tracing the response of Ultra-High performance concrete beams exposed to fire. *Fire Mater.* **2023**, *47*, 322–340. [[CrossRef](#)]
40. Sadaghian, H.; Pourbaba, M.; Andabili, S.Z.; Mirmiran, A. Experimental and numerical study of flexural properties in UHPFRC beams with and without an initial notch. *Constr. Build. Mater.* **2021**, *268*, 121196. [[CrossRef](#)]
41. Liu, Y.; Xie, J.; Yan, J.B. Flexural and fracture performance of UHPC exposed to low-temperature environment. *Constr. Build. Mater.* **2023**, *373*, 130865. [[CrossRef](#)]
42. Al-Osta, M.A.; Kharma, K.M.; Ahmad, S.; Maslehuddin, M.; Al-Huri, M.; Khalid, H. Strategies for strengthening of corroded reinforced concrete beams using CFRP laminates and UHPC jacketing. *Struct. Concr.* **2023**, *24*, 1546–1571. [[CrossRef](#)]
43. Hong, S.G.; Lim, W.Y. Strengthening of shear-dominant reinforced concrete beams with ultra-high-performance concrete jacketing. *Constr. Build. Mater.* **2023**, *365*, 130043. [[CrossRef](#)]
44. Zmetra, K.M.; McMullen, K.F.; Zaghi, A.E.; Wille, K. Experimental study of UHPC repair for corrosion-damaged steel girder ends. *J. Bridge Eng.* **2017**, *22*, 04017037. [[CrossRef](#)]
45. Zhang, Y.; Zhu, P.; Liao, Z.; Wang, L. Interfacial bond properties between normal strength concrete substrate and ultra-high performance concrete as a repair material. *Constr. Build. Mater.* **2020**, *235*, 117431. [[CrossRef](#)]
46. Liu, Y.; Wei, Y. Effect of calcined bauxite powder or aggregate on the shrinkage properties of UHPC. *Cem. Concr. Compos.* **2021**, *118*, 103967. [[CrossRef](#)]
47. Smarzewski, P. Mechanical properties of ultra-high performance concrete with partial utilization of waste foundry sand. *Buildings* **2020**, *10*, 11. [[CrossRef](#)]
48. Du, J.; Meng, W.; Khayat, K.H.; Bao, Y.; Guo, P.; Lyu, Z.; Abu-Obeidah, A.; Nassif, H.; Wang, H. New development of ultra-high-performance concrete (UHPC). *Compos. Part B Eng.* **2021**, *224*, 109220. [[CrossRef](#)]
49. Pyo, S.; Abate, S.Y.; Kim, H.K. Abrasion resistance of ultra high performance concrete incorporating coarser aggregate. *Constr. Build. Mater.* **2018**, *165*, 11–16. [[CrossRef](#)]
50. Li, P.P.; Yu, Q.L.; Brouwers, H.J.; Chen, W. Conceptual design and performance evaluation of two-stage ultra-low binder ultra-high performance concrete. *Cem. Concr. Res.* **2019**, *125*, 105858. [[CrossRef](#)]
51. Pyo, S.; Kim, H.K.; Lee, B.Y. Effects of coarser fine aggregate on tensile properties of ultra high performance concrete. *Cem. Concr. Compos.* **2017**, *84*, 28–35. [[CrossRef](#)]
52. Yoo, D.Y.; Kim, M.J.; Kim, S.W.; Park, J.J. Development of cost effective ultra-high-performance fiber-reinforced concrete using single and hybrid steel fibers. *Constr. Build. Mater.* **2017**, *150*, 383–394. [[CrossRef](#)]
53. Meng, W.; Yao, Y.; Mobasher, B.; Khayat, K.H. Effects of loading rate and notch-to-depth ratio of notched beams on flexural performance of ultra-high-performance concrete. *Cem. Concr. Compos.* **2017**, *83*, 349–359. [[CrossRef](#)]
54. ASTM C494/C494M; Standard Specification for Chemical Admixtures for Concrete. ASTM International: West Conshohocken, PA, USA, 2019.
55. ASTM C39/C39M; Standard Test Method for Compressive Strength of Cylindrical Concrete Specimens. ASTM International: West Conshohocken, PA, USA, 2021.

56. SETRA Service d'études Techniques des Routes et Autoroutes; AFGC Association Française de Génie Civil. *Ultra High Performance Fiber-Reinforced Concretes-Interim Recommendations Bétons Fibrés à UltraHautes Performances-Recommandations Provisoires*; SETRA: Paris, France, 2002.
57. *ASTM C1609/C1609M*; Standard Test Method for Flexural Performance of Fiber-Reinforced Concrete (Using Beam with Third-Point Loading). ASTM International: West Conshohocken, PA, USA, 2019.
58. ATENA. *Finite Element Software, ATENA Program Documentation, Theory and FRC User Manual*; Cervenka Consulting: Prague, Czech Republic, 2016.
59. GID. *Pre-, and Post-Processing Software for Engineering Models*; International Centre for Numerical Methods in Engineering CIMNE: Barcelona, Spain, 2015.
60. Khalilzadehtabrizi, S.; Sadaghian, H.; Farzam, M. Uncertainty of concrete strength in shear and flexural behavior of beams using lattice modeling. *Front. Struct. Civ. Eng.* **2023**, *17*, 306–325. [[CrossRef](#)]
61. Sadaghian, H.; Farzam, M. Numerical investigation on punching shear of RC slabs exposed to fire. *Comput. Concr.* **2019**, *23*, 217–233.
62. Dadmand, B.; Sadaghian, H.; Khalilzadehtabrizi, S.; Pourbaba, M.; Shirdel, M.; Mirmiran, A. Studying the compressive, tensile and flexural properties of binary and ternary fiber-reinforced UHPC using experimental, numerical and multi-target digital image correlation methods. *Case Stud. Constr. Mater.* **2023**, *2023*, e01865. [[CrossRef](#)]
63. Dadmand, B.; Pourbaba, M.; Sadaghian, H.; Mirmiran, A. Experimental & numerical investigation of mechanical properties in steel fiber-reinforced UHPC. *Comput. Concr. Int. J.* **2020**, *26*, 451–465.
64. Dadmand, B.; Pourbaba, M.; Sadaghian, H.; Mirmiran, A. Effectiveness of steel fibers in ultra-high-performance fiber-reinforced concrete construction. *Adv. Concr. Constr.* **2020**, *10*, 195–209.
65. Parvin, Y.A.; Shaghaghi, T.M.; Pourbaba, M.; Mirrezaei, S.S.; Zandi, Y. Experimental investigation on UHPC beams reinforced with GFRP and steel rebars and comparison with prediction equations. *Adv. Concr. Constr.* **2022**, *14*, 45–55.
66. Dadmand, B.; Pourbaba, M.; Riahi, R. Experimental and Numerical Investigation of Different Types of Jacketing Effect on Retrofitting RC Short Columns Using ECC Concrete. *Period. Polytech. Civ. Eng.* **2022**, *66*, 603–613. [[CrossRef](#)]
67. Ahangarnazha, B.H.; Pourbaba, M.; Afkar, A. Bond behavior between steel and Glass Fiber Reinforced Polymer (GFRP) bars and ultra high performance concrete reinforced by Multi-Walled Carbon Nanotube (MWCNT). *Steel Compos. Struct. Int. J.* **2020**, *35*, 463–474.
68. Baghaei Osgouei, Y.; Tavousi Tafreshi, S.; Pourbaba, M. Flexural Properties of UHPFRC Beams with an Initial Notch. *J. Rehabil. Civ. Eng.* **2023**, *11*, 141–177.
69. Pourbaba, M.; Joghataie, A. Determining shear capacity of ultra-high performance concrete beams by experiments and comparison with codes. *Sci. Iran.* **2019**, *26*, 273–282. [[CrossRef](#)]
70. Suksawang, N.; Wtaife, S.; Alsabbagh, A. Evaluation of Elastic Modulus of Fiber-Reinforced Concrete. *ACI Mater. J.* **2018**, *115*, 239–249. [[CrossRef](#)]
71. Bazant, Z.P.; Chen, E.P. Scaling of structural failure. *Appl. Mech. Rev.* **1997**, *50*, 593. [[CrossRef](#)]
72. Carpinteri, A.; Chiaia, B. Multifractal scaling laws in the breaking behaviour of disordered materials. *Chaos Solitons Fractals* **1997**, *8*, 135–150. [[CrossRef](#)]
73. Kim, J.K.; Yi, S.T. Application of size effect to compressive strength of concrete members. *Sadhana* **2002**, *27*, 467–484. [[CrossRef](#)]
74. Skazlić, M.; Bjegović, D. Toughness testing of ultra high performance fibre reinforced concrete. *Mater. Struct.* **2009**, *42*, 1025–1038. [[CrossRef](#)]
75. Walraven, J.C. High performance fiber reinforced concrete: Progress in knowledge and design codes. *Mater. Struct.* **2009**, *42*, 1247. [[CrossRef](#)]

**Disclaimer/Publisher's Note:** The statements, opinions and data contained in all publications are solely those of the individual author(s) and contributor(s) and not of MDPI and/or the editor(s). MDPI and/or the editor(s) disclaim responsibility for any injury to people or property resulting from any ideas, methods, instructions or products referred to in the content.